



## Stick-Slip Motion of the Wigner Solid on Liquid Helium

David G. Rees,<sup>1,2,\*</sup> Niyaz R. Beysengulov,<sup>2,3</sup> Juhn-Jong Lin,<sup>1,2,4</sup> and Kimitoshi Kono<sup>1,2,3</sup>

<sup>1</sup>*NCTU-RIKEN Joint Research Laboratory, Institute of Physics, National Chiao Tung University, Hsinchu 300, Taiwan*

<sup>2</sup>*RIKEN CEMS, Wako 351-0198, Japan*

<sup>3</sup>*KFU-RIKEN Joint Research Laboratory, Institute of Physics, Kazan Federal University, Kazan 420008, Russia*

<sup>4</sup>*Department of Electrophysics, National Chiao Tung University, Hsinchu 300, Taiwan*

(Received 28 October 2015; revised manuscript received 17 March 2016; published 16 May 2016)

We present time-resolved transport measurements of a Wigner solid (WS) on the surface of liquid helium confined in a micron-scale channel. At rest, the WS is “dressed” by a cloud of quantized capillary waves (ripples). Under a driving force, we find that repeated WS-ripple decoupling leads to stick-slip current oscillations, the frequency of which can be tuned by adjusting the temperature, pressing electric field, or electron density. The WS on liquid He is a promising system for the study of polaronlike decoupling dynamics.

DOI: 10.1103/PhysRevLett.116.206801

Surface-state electrons (SSEs) on liquid helium substrates (Fig. 1) form a model Coulomb system [1], the ground state of which remains the clearest example of the classical Wigner solid (WS) [2]. The WS is dressed by a cloud of ripples, the Bragg scattering of which from the electron lattice gives rise to a commensurate deformation of the He surface known as the dimple lattice (DL) [3–6]. The WS-DL system is analogous to polaron states in which electrons are dressed by a cloud of virtual phonons, or lattice deformation [7–9]. On liquid He individual electrons do not perform self-trapping; rather, the DL appears as a consequence of the long-range electron ordering. Also, the lattice constant of the WS (and so the DL) is no less than 100 nm, and a continuum description of the medium (liquid He) is applicable. Despite these differences, the decoupling dynamics of the WS and polaron systems exhibit strong similarities [10,11], although the rate depends on the different binding energies; polaron decoupling in a GaAs crystal occurs in the femtosecond range [12], whereas the decoupling of the WS from the DL takes place on nanosecond time scales. It is therefore more straightforward to observe the real-time decoupling for the WS than for polarons.

In contrast to other systems, the coupling of the WS with the DL is of a dynamical nature, due to a resonant interaction between the WS and ripples emitted by the moving electron lattice. According to hydrodynamic theory, when the WS is at rest the depth of the surface dimples  $\xi_0$  can be estimated as

$$\xi_0 \approx -\frac{\sqrt{3}eE_z}{8\pi^2\sigma} e^{-W}, \quad (1)$$

where  $e$ ,  $E_z$ ,  $\sigma$ , and  $e^{-W}$  are the elementary charge, perpendicular pressing electric field, surface tension coefficient of liquid He, and the self-consistent Debye-Waller

factor, respectively [13]. Typically,  $\xi_0 \approx 10^{-12}$  m. However, when the velocity of the WS-DL system approaches the phase velocity of ripples of wave vector equal to the WS periodicity,  $v_{BC}$ , constructive interference resonantly deepens the DL. As a result, the resistive force exerted on the WS increases dramatically. This is called the Bragg-Cherenkov (BC) effect [14–16]. The decoupling of the WS therefore occurs from this dynamically pinned state and, hence, under strongly nonequilibrium conditions. Thus far, however, very little is known about this decoupling process. It is an interesting problem concerning strongly correlated systems far from equilibrium, and also from a hydrodynamics point of view.

The WS decoupling from the DL was first observed in Corbino conductivity measurements under perpendicular magnetic fields [17]. The decoupling was signaled by an abrupt jump in conductivity on sweeping the amplitude or frequency of the sinusoidal driving potential, or the magnetic field, and so on [18]. In such experiments, magnetic fields are necessary because an electric field large enough to cause the decoupling cannot be applied to the WS due to its high mobility. The electric current then flows azimuthally, whereas the electric field acts in the radial direction. The Hall angle is almost 90 deg, and, hence, the azimuthal current or velocity of the SSEs is extremely difficult to determine. Furthermore, the electric field is spatially inhomogeneous and time varying. These

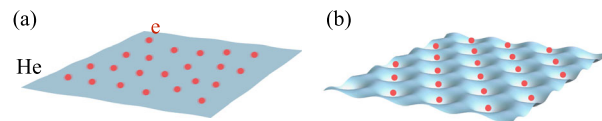


FIG. 1. Schematic depiction of electrons on the surface of liquid helium. (a) Above  $T_m$  electrons move freely in the 2D plane above the surface. (b) Below  $T_m$  the Wigner solid is dressed by capillary waves, giving rise to the dimple lattice.

ambiguities make analysis of the decoupling process difficult.

Recently, SSEs in capillary-condensed microchannel devices have been found to show the decoupling phenomena without applying magnetic fields [19]. In such devices the electric current is homogeneous but is typically measured using a sinusoidal driving voltage. The transport measurement is then inevitably complicated by the non-linear response of the WS during each ac cycle. In this Letter we report simultaneous measurements of the WS velocity and driving electric field by employing a linear sweep of the driving electric potential. That is, we performed the first time-resolved transport measurement of a quasi-1D WS confined in a microchannel. We demonstrate that, under a driving potential, repeated ripplon dressing and decoupling causes stick-slip motion of the WS and thus oscillations of the electron velocity. Our experiment allows the control and quantitative analysis of the decoupling dynamics of the WS.

The device used in the experiment is shown in Fig. 2(b). Our sample is electrons floating on a helium surface in a microchannel  $7.5 \mu\text{m}$  wide,  $100 \mu\text{m}$  long, and  $h = 2.2 \mu\text{m}$  deep. We denote this the central microchannel (CM). Two large arrays of microchannels, which act as electron reservoirs, are attached to the CM. The SSE in the reservoirs are capacitively coupled to the external circuit by  $C_l$  and  $C_r$ , as shown schematically in Fig. 2(a). To

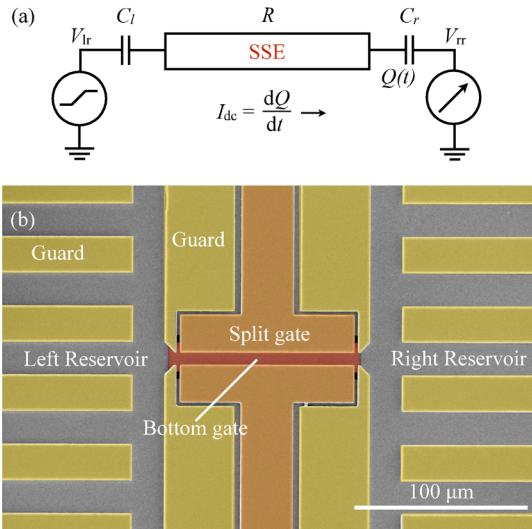


FIG. 2. (a) Schematic circuit diagram of the dc current measurement. The SSEs in the CM form an electrical resistance  $R$ . The electron system is coupled to the external circuit by the capacitances  $C_l$  and  $C_r$ . The current  $I_{dc}$  flows through the CM in response to varying  $V_{lr}$ , resulting in the transfer of charge  $Q(t)$  from the left to the right reservoir, which accumulates in  $C_l$  and  $C_r$ . The capacitive coupling to the guard electrode is omitted for simplicity. (b) False-color scanning electron micrograph of a sample identical to those used in the experiment. The left and right reservoirs each contain 25 microchannels of length  $0.7 \text{ mm}$  connected in parallel.

measure SSE transport through the CM, the voltage  $V_{lr}$  applied to the electrode beneath the He in the left reservoir (left reservoir electrode) was ramped from 0 to  $+50 \text{ mV}$  in a time  $t_r$ . As  $V_{lr}$  is varied, charge moves between the reservoirs. After the ramp period, the charge distribution achieves a new equilibrium state and the current stops. To determine the charge accumulated in  $C_l$  and  $C_r$ , and thus the SSE current  $I_{dc}$  passing through the CM, the current flowing in the electrode beneath the He in the right reservoir (right reservoir electrode,  $V_{rr} = 0 \text{ V}$ ) was recorded. To tune the electrostatic confinement for SSEs in the CM, voltages  $V_{bg}$  and  $V_{sg}$  were applied to the electrode beneath the He in the CM (bottom gate electrode) and the electrode in the plane of the He surface (split gate electrode), respectively. The voltage on the guard electrode was  $-0.2 \text{ V}$ .

The current measurement was performed using a current preamplifier and a digital storage oscilloscope. The measurement was averaged over several thousand cycles. A small current component due to cross talk between the electrical cables was subtracted from the measurement. The bandwidth of the preamplifier was  $200 \text{ kHz}$ , which leads to the smoothing of some of the transport features shown here but does not detract from the essential physics. Finite-element modeling (FEM) [20] was used to calculate the average areal electron density  $n_s$  ( $\text{m}^{-2}$ ), the electrostatic potential of the electron system  $V_e$  (which depends on  $n_s$ ), the effective width  $w_e$  of the charge sheet in the CM, the linear electron density  $n_l$  ( $\text{m}^{-1}$ ), and the number of electron rows  $N_y$ , for varying bias conditions [21,22].

Results of transient current measurements are shown in Fig. 3 for  $t_r = 20 \mu\text{s}$ ,  $V_{sg} = -0.2 \text{ V}$ . Generally, current flows in the CM in response to the  $V_{lr}$  ramp. However, the transport is strongly influenced by  $V_{bg}$ , the value of which

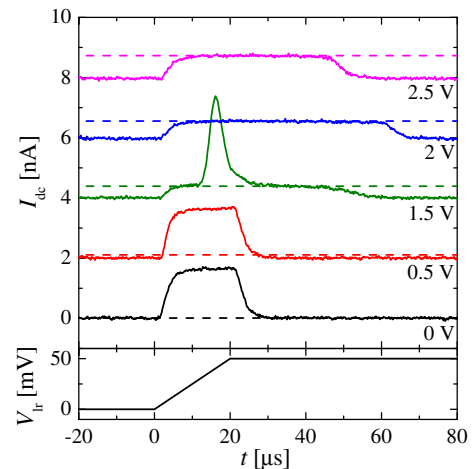


FIG. 3.  $I_{dc}$  against time  $t$  for  $V_{sg} = -0.2 \text{ V}$  and different values of  $V_{bg}$  as indicated on the plot. Here,  $T = 0.6 \text{ K}$ . Each data set is shifted vertically by  $2 \text{ nA}$  for clarity. The dashed lines indicate the value of  $I_{BC}$  expected for each value of  $V_{bg}$ . The lower panel shows the  $V_{lr}$  voltage waveform.

determines the electron density in the CM. The WS forms when the ratio of the electron Coulomb energy to kinetic energy  $\Gamma = E_C/E_k = e^2\sqrt{\pi n_s}/4\pi\epsilon_0 k_B T$  reaches a threshold value of  $\sim 130$ , where  $\epsilon_0$ ,  $k_B$ , and  $T$  are the vacuum permittivity, the Boltzmann constant, and the temperature, respectively [2]. At the experimental temperature  $T = 0.6$  K, the WS should form when  $n_s \approx 7.1 \times 10^{12} \text{ m}^{-2}$ , which occurs when  $V_{\text{bg}} = 0.18$  V, according to the FEM [22]. It is clear that for both the electron liquid ( $V_{\text{bg}} = 0$  V) and the low-density WS ( $V_{\text{bg}} = 0.5$  V) a constant current flows in the CM as  $V_{\text{lr}}$  changes. For  $V_{\text{bg}} = 1.5$  V, the current is initially suppressed but then suddenly increases, during the  $V_{\text{lr}}$  ramp, before relaxing. For  $V_{\text{bg}} = 2.0$  and  $2.5$  V,  $I_{\text{dc}}$  is small and continues to flow after the ramp phase.

Because the SSE system is capacitively coupled to both the reservoir and guard electrodes, the measurement of the current registered on the right reservoir electrode does not give the true current flowing in the CM. The average charge detected by integrating the current measurements shown in Fig. 3 is  $Q^{\text{av}} = 1.58 \times 10^5 e$ , with standard deviation  $0.04 \times 10^5 e$ . The FEM analysis gives the expected value  $Q^{\text{FEM}} = 2.03 \times 10^5 e$ . The deficit is due to the displacement current flowing into the guard electrode. In Figs. 3 and 4, the current measurement is therefore corrected by the factor  $Q^{\text{FEM}}/Q^{\text{av}} = 1.28$ .

BC scattering followed by WS-DL decoupling results in an abrupt jump in the WS conductivity with increasing driving force. The influence of BC scattering on the WS velocity in the CM can be estimated using the periodicity of the WS along the channel,  $a = N_y/n_l$ . The limiting

velocity is given by  $v_{\text{BC}} = (\sigma k/\rho)^{1/2}$ , where the wave vector  $k = 2\pi/a$  and  $\rho$  is density of liquid He. The typical electron spacing is 300 nm, and therefore  $kh \gg 1$ . In this ‘‘thick-film’’ limit the dispersion relation for ripplons on bulk liquid He  $\omega^2 = (\sigma/\rho)k^3$  is applicable. The BC scattering-limited current was calculated as  $I_{\text{BC}} = n_l e v_{\text{BC}}$  for the bias conditions in Figs. 3 and 4.

On comparing  $I_{\text{BC}}$  with the measurements in Fig. 3, it is clear that when  $V_{\text{bg}}$  is sufficiently large, the WS is pinned to the DL and, due to BC scattering,  $I_{\text{dc}} = I_{\text{BC}}$ . Then, because  $I_{\text{dc}}$  is limited, the potential difference between the left and right reservoirs builds up during the  $V_{\text{lr}}$  ramp and the current continues to flow after the ramp phase. For  $V_{\text{bg}} = 1.5$  V, the electron velocity is initially limited by the BC scattering, but as the potential difference builds, it suddenly increases when the electrons decouple from the DL. This releases the force and the electron velocity quickly returns to  $v_{\text{BC}}$ . For  $V_{\text{bg}} = 0.5$  V, the driving force always overcomes the weaker pinning and the current exceeds  $I_{\text{BC}}$ .

The stronger pinning of the WS with increasing  $V_{\text{bg}}$  is expected, as  $n_s$  (and so  $\Gamma$ ) and  $E_z$  both increase with  $V_{\text{bg}}$ . However, by keeping the electrode bias conditions fixed and changing temperature, the influence of the electron thermal motion on the WS decoupling can be determined unambiguously. Approaching the WS melting point, thermal fluctuations in the electron positions should degrade the DL, leading to a decrease in the decoupling threshold force. This in turn should lead to a decrease in the time taken for the decoupling to occur in our transport measurements. In Fig. 4(a) we show  $I_{\text{dc}}$  against time  $t$  at different temperatures. Here,  $t_r = 80 \mu\text{s}$ . The split gate voltage was  $V_{\text{sg}} = -1$  V, which reduces  $n_s$  and  $w_e$ . This increases the resistance of the SSE system  $R$  and thereby slows the system response to the  $V_{\text{lr}}$  ramp [see Fig. 2(a)]. During the ramp phase, multiple decoupling events occur, at regular intervals. After each decoupling event  $I_{\text{dc}}$  returns to  $I_{\text{BC}}$  and the stick-slip cycle is repeated. For increasing  $T$  (decreasing  $\Gamma$ ) the stick-slip period decreases as the time taken to reach the decoupling threshold force is reduced.

Similar narrow band current oscillations, also attributed to WS sliding, have been observed for degenerate electron systems in the WS regime [23]. However, for such cases little is known about the nature of the collective electron ground states or the mechanisms by which pinning forces are overcome. Qualitatively similar phenomena are observed in charge or spin density wave systems. But, contrary to those systems, the present system does not have a pinning mechanism due to irregularities. In our experiments, the quantitative understanding of the BC scattering mechanism allows us to clearly demonstrate the link between WS sliding and the appearance of spontaneous current oscillations.

Stick-slip motion typically results in a sawtooth-type force-velocity profile [24]. For the data shown in Fig. 4(a),

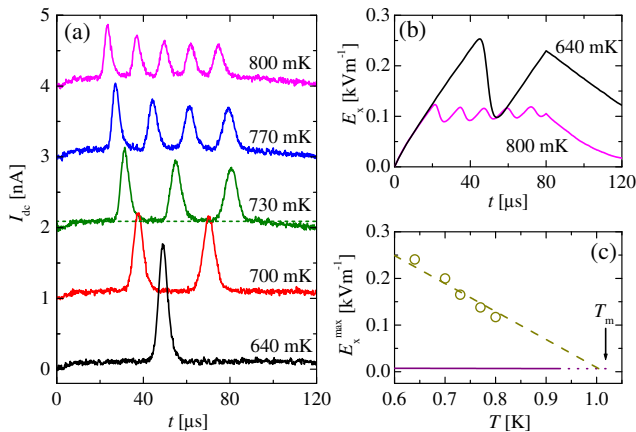


FIG. 4. (a)  $I_{\text{dc}}$  against time  $t$  at different temperatures from 640 to 800 mK, as indicated on the plot. Here,  $t_r = 80 \mu\text{s}$ ,  $V_{\text{bg}} = 1.2$  V, and  $V_{\text{sg}} = -1$  V. Each data set is shifted by 1 nA for clarity. For  $T = 730$  mK, we plot the expected  $I_{\text{BC}}$  (dashed line). (b)  $E_x$  against  $t$  for the data shown in (a) for  $T = 640$  and  $800$  mK. (c)  $E_x^{\text{max}}$  against  $T$ , for the data shown in (a). The dashed line is a guide to the eye. The solid and dotted line indicates the value of  $E_x^{\text{max}}$  expected for a dimple depth  $\xi_0$ .  $T_m = 1.02$  K is indicated by the arrow.

to calculate the time-varying electric field along the CM,  $E_x(t)$ , we integrate  $I_{dc}$  at each value of  $t$  to obtain the charge accumulated in the right reservoir  $Q(t)$ . Analysis of the circuit diagram in Fig. 2(a) gives  $E_x(t) = [V_{lr}(t) - V_{rr} - 2Q(t)/C]/l$ , where  $l = 100 \mu\text{m}$ , and  $C = C_l = C_r = 1.01 \text{ pF}$  is given by the measurement of  $Q_{av}$ . In Fig. 4(b) we show the dependence of  $E_x$  on  $t$ , at  $T = 800$  and  $640 \text{ mK}$ . The driving field builds steadily when the WS is pinned by the DL and then drops rapidly as the WS decouples. The maximum value of the driving field  $E_x^{\text{max}}$  is higher at lower temperature, as expected. For this measurement, the FEM gives  $n_s = 2.04 \times 10^{13} \text{ m}^{-2}$ , for which the melting temperature  $T_m = 1.02 \text{ K}$ . As shown in Fig. 4(c),  $E_x^{\text{max}}$  extrapolates close to this value, as the decoupling force becomes zero when the WS melts.

Assuming a sinusoidal surface profile, equating the components of the forces acting on each electron in the direction of motion yields the expression  $k\xi_{\text{th}} = E_x^{\text{max}}/E_z$ , where  $\xi_{\text{th}}$  is the dimple depth at the decoupling threshold. The  $E_x^{\text{max}}$  expected for the static DL ( $\xi_{\text{th}} = \xi_0$ ) is shown in Fig. 4(c). (Note that the dependence of  $\xi_0$  on  $T$  is weak, without taking the WS melting into account.) As expected, the experimental values of  $E_x^{\text{max}}$  are larger than those for the static DL, as a consequence of the resonant deepening of the DL due to BC scattering. For  $T = 0.64 \text{ K}$ , we estimate  $E_x^{\text{max}}/E_z = 1.4 \times 10^{-3}$ ,  $a = 240 \text{ nm}$ , and thus  $\xi_{\text{th}} = 5.2 \times 10^{-11} \text{ m}$ . This value exceeds the static dimple depth  $\xi_0 \approx 2 \times 10^{-12} \text{ m}$ , and is consistent with other measurements [19].

For the bulk 2D WS the magnitude of the WS-DL coupling is estimated by  $eE_z\xi_0$  [Eq. (1)]. Since  $E_z$  and  $W$  are functions of  $V_{bg}$ , the decoupling threshold depends on  $V_{bg}$ , yet the dependence should be monotonic and smooth. In Fig. 5 we show  $I_{dc}$  against  $t$ , recorded for  $V_{bg}$  values between  $0.85$  and  $1.10 \text{ V}$ . Here,  $t_r = 80 \mu\text{s}$ ,  $V_{sg} = -1 \text{ V}$ , and  $T = 0.6 \text{ K}$ . The time values at which  $I_{dc}$  reaches its peak value  $t_p$  are plotted in the inset. Although the general trend, the increase of the decoupling threshold, is as expected, it is remarkably tortuous. We ascribe this effect to successive structural transitions of electron row formation. The numbers of electron rows along the quasi-1D channel, as calculated by the FEM, are indicated in the inset of Fig. 5. Clear correspondence is observed. Previous (ac) measurements have shown a similar modulation effect due to the reduced positional order of the WS at each structural boundary [21,25]. Further details of the influence of confinement on the WS ordering will be reported elsewhere.

Stick-slip motion is common in nature, although complex microscopic processes often determine macroscopic motion [26–28]. Here, for SSEs in a microchannel confinement, we have demonstrated a quantitative understanding of stick-slip friction at a microscopic level and that the coupling between the WS and the He substrate depends on the positional ordering of the quasi-1D electron system.

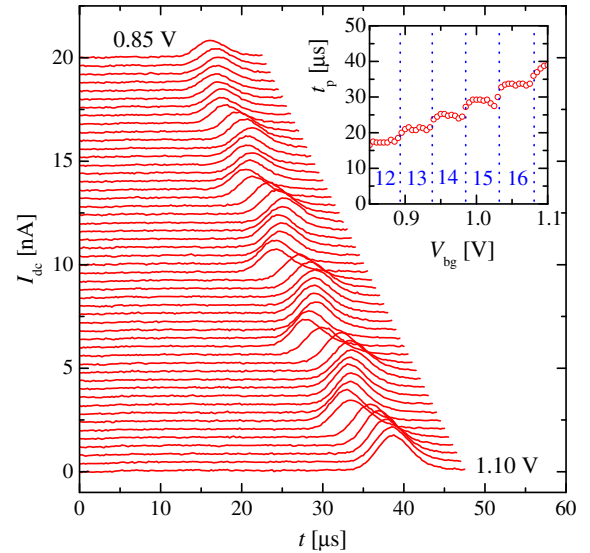


FIG. 5.  $I_{dc}$  against  $t$  for different values of  $V_{bg}$ .  $V_{bg}$  is varied from  $1.10$  to  $0.85 \text{ V}$  in  $5 \text{ mV}$  steps. Each data set is shifted by  $0.4 \text{ nA}$  for clarity. Inset: The corresponding values of the  $I_{dc}$  peak position  $t_p$  against  $V_{bg}$ . The dotted lines mark the values of  $V_{bg}$  at which structural transitions between electron row configurations occur, as calculated by the FEM. The values of  $N_y$  between each transition are indicated.

Recently, quasi-1D cold ion systems comprising less than  $10$  particles have been used to investigate the influences of dimensionality and commensurability on sliding friction [29]. Our results demonstrate that similar investigations can be conducted with quasi-1D SSE systems, which can contain a much larger number of particles, by measuring decoupling from the DL or from lithographically structured substrates.

In conclusion, we have presented the first demonstration of stick-slip motion of the WS on a liquid He substrate. Our microchannel device allows precise control and quantitative analysis of the WS decoupling, which exhibits basic similarities with polaron dynamics. SSEs on He are a promising system to study stick-slip friction at the nanoscale.

We are grateful to M. I. Dykman for helpful discussions. This work was supported by JSPS KAKENHI Grant No. 24000007, and by the Taiwan Ministry of Science and Technology (MOST) through Grants No. NSC 102-2112-M-009-015 and No. MOST 103-2112-M-009-017 and the Taiwan Ministry of Education (MOE) ATU Plan. This work was performed according to the Russian Government Program of Competitive Growth of Kazan Federal University.

\*drees@nctu.edu.tw

[1] *Two-Dimensional Electron Systems on Helium and Other Cryogenic Substrates*, edited by E. Y. Andrei *et al.* (Kluwer Academic, Dordrecht, 1997).

- [2] C. C. Grimes and G. Adams, *Phys. Rev. Lett.* **42**, 795 (1979).
- [3] Y. P. Monarkha and V. B. Shikin, *Sov. Phys. JETP* **41**, 710 (1975).
- [4] D. S. Fisher, B. I. Halperin, and P. M. Platzman, *Phys. Rev. Lett.* **42**, 798 (1979).
- [5] M. Saitoh, *J. Phys. Soc. Jpn.* **55**, 1311 (1986).
- [6] P. Leiderer, W. Ebner, and V. B. Shikin, *Surf. Sci.* **113**, 405 (1982).
- [7] A. S. Alexandrov and J. T. Devreese, *Advances in Polaron Physics* (Springer, New York, 2010).
- [8] M. I. Dykman and E. I. Rashba, *Phys. Today* **68**, No. 4, 10 (2015).
- [9] E. Y. Andrei, *Phys. Rev. Lett.* **52**, 1449 (1984).
- [10] A. A. Johansson and S. Stafström, *Phys. Rev. B* **69**, 235205 (2004).
- [11] N.-H. Ge, C. Wong, R. Lingle, J. McNeill, K. Gaffney, and C. Harris, *Science* **279**, 202 (1998).
- [12] P. Gaal, W. Kuehn, K. Reimann, M. Woerner, T. Elsaesser, and R. Hey, *Nature (London)* **450**, 1210 (2007).
- [13] Y. P. Monarkha and K. Kono, *J. Phys. Soc. Jpn.* **74**, 960 (2005).
- [14] M. I. Dykman and Y. G. Rubo, *Phys. Rev. Lett.* **78**, 4813 (1997).
- [15] W. F. Vinen, *J. Phys. Condens. Matter* **11**, 9709 (1999).
- [16] A. Kristensen, K. Djerfi, P. Fozooni, M. J. Lea, P. J. Richardson, A. Santrich-Badal, A. Blackburn, and R. W. van der Heijden, *Phys. Rev. Lett.* **77**, 1350 (1996).
- [17] K. Shirahama and K. Kono, *Phys. Rev. Lett.* **74**, 781 (1995).
- [18] K. Shirahama and K. Kono, *J. Low Temp. Phys.* **104**, 237 (1996).
- [19] H. Ikegami, H. Akimoto, and K. Kono, *Phys. Rev. Lett.* **102**, 046807 (2009).
- [20] F. Hecht, *J. Numer. Math.* **20**, 251 (2012).
- [21] N. R. Beysengulov, D. G. Rees, Y. Lysogorskiy, N. K. Galiullin, A. S. Vazjukov, D. A. Tayurskii, and K. Kono, *J. Low Temp. Phys.* **182**, 28 (2016).
- [22] See Supplemental Material at <http://link.aps.org/supplemental/10.1103/PhysRevLett.116.206801> for details of the experimental method, electrostatic modeling, and ac transport measurements used to characterize the device.
- [23] G. A. Csáthy, D. C. Tsui, L. N. Pfeiffer, and K. W. West, *Phys. Rev. Lett.* **98**, 066805 (2007).
- [24] B. N. J. Persson, *Sliding Friction: Physical Principles and Applications* (Springer Science and Business Media, Berlin, Heidelberg, 2000), Vol. 1.
- [25] H. Ikegami, H. Akimoto, D. G. Rees, and K. Kono, *Phys. Rev. Lett.* **109**, 236802 (2012); D. G. Rees, H. Ikegami, and K. Kono, *J. Phys. Soc. Jpn.* **82**, 124602 (2013).
- [26] A. Vanossi, N. Manini, M. Urbakh, S. Zapperi, and E. Tosatti, *Rev. Mod. Phys.* **85**, 529 (2013).
- [27] C. Lee, Q. Li, W. Kalb, X.-Z. Liu, H. Berger, R. W. Carpick, and J. Hone, *Science* **328**, 76 (2010).
- [28] M. Lee, B. Kim, J. Kim, and W. Jhe, *Nat. Commun.* **6**, 7359 (2015).
- [29] A. Bylinskii, D. Gangloff, and V. Vuletić, *Science* **348**, 1115 (2015).